Morphometric Model for Discrimination between Glioblastoma Multiforme and Solitary Metastasis Using Three-Dimensional Shape Analysis

Guang Yang,* Timothy L. Jones, Franklyn A. Howe, and Thomas R. Barrick

Purpose: Glioblastoma multiforme (GBM) and brain metastasis (MET) are the most common intra-axial brain neoplasms in adults and often pose a diagnostic dilemma using standard clinical MRI. These tumor types require different oncological and surgical management, which subsequently influence prognosis and clinical outcome.
Methods: Here, we hypothesize that GBM and MET possess different three-dimensional (3D) morphological attributes based on their physical characteristics. A 3D morphological analysis was applied on the tumor surface defined by our diffusion tensor imaging (DTI) segmentation technique. It segments the DTI data into clusters representing different isotropic and anisotropic water diffusion characteristics, from which a distinct surface boundary between healthy and pathological tissue was identified. Morphometric features of shape index and curvedness were then computed for each tumor surface and used to build a morphometric model of GBM and MET pathology with the goal of developing a tumor classification method based on shape characteristics.
Results: Our 3D morphometric method was applied on 48 untreated brain tumor patients. Cross-validation resulted in a 95.8% accuracy classification with only two shape features needed and that can be objectively derived from quantitative imaging methods.
Conclusion: The proposed 3D morphometric analysis framework can be applied to distinguish GBMs from solitary METs. Magn Reson Med 75:2505–2516, 2016. © 2015 Wiley Periodicals, Inc.

Key words: brain tumor classification; diffusion tensor imaging segmentation; computer-aided diagnosis; pattern recognition and classification; shape analysis; magnetic resonance imaging

INTRODUCTION

Glioblastoma multiforme (GBM) and brain metastasis (MET) are common malignant brain tumors in adults, that produce similar clinical symptoms but have different treatment strategies (1,2) and, hence, require an accurate diagnosis. GBMs are infiltrative tumors which inhibits a 100% surgical resection and with current surgery and adjuvant therapy there is a median survival time of typically 12–14 months (3). METs have a more encapsulated growth and median survival time of patients is short (1–2 months with corticosteroids) (4) but may be extended to 10.7 months with whole brain radiation therapy (5).

Diagnosis of brain MET may be based on the multiplicity of lesions or the clinical history of systemic cancer (6); however, it is problematic when the lesion is solitary and clinical findings are noncontributory (7). In approximately one-quarter to one-third of cases, cerebral MET presents as a solitary lesion (8), and in approximately 15% of cases, a MET is detected without evidence of disease elsewhere in the body (9). This scenario can pose a diagnostic dilemma with conventional clinical MRI as the appearance of MET is similar to GBM (10): both can present with necrotic features (11), ring-enhancement, and extensive edema (12).

The gold standard for establishing the diagnosis of GBM or MET is histopathological analysis of a biopsy sample; however, differentiation by a noninvasive method is beneficial when the mass is located near an eloquent area or when a biopsy procedure could result in significant morbidity due to the patient's advanced age. Because conventional structural MRI is ambiguous advanced techniques such as MR spectroscopy (7,13,14), perfusion MR (10,15) and diffusion tensor imaging (DTI) (6,16), have been investigated for their accuracy in differentiation of GBM from solitary MET.

Based on conventional structural and advanced MRI, a variety of sophisticated methods have been investigated to aid discrimination of GBMs and METs. For example, advanced ensemble learning applied with texture analysis achieved only 77% accuracy for distinguishing METs (17) due to similar appearance of GBMs and solitary METs on conventional structural MR images, texture features highly overlap in the feature space.

MR spectroscopy and perfusion MR have both been shown to provide good discrimination (classification accuracy of 60–80%) between GBMs and solitary METs, e.g., (14) and (10); however, both techniques require subjective definition of tumor and/or peritumor regions of interest (ROIs). In addition, both single-voxel and multi-voxel MR spectroscopy acquisitions require careful planning to avoid artefacts from scalp lipid signals, distortions by water signals from cerebrospinal fluid, and poor spectral quality due to B_0 inhomogeneity in regions near to sinuses; thereby MRS can be more limited in whole brain coverage than MRI methods. For perfusion

*Correspondence to: Guang Yang, Ph.D., Neuroscience Research Centre, Cardiovascular and Cell Sciences Institute, St George's, University of London, Cranmer Terrace, London, SW17 0RE. E-mail: gyang@sgul.ac.uk

studies, measurement ROIs need to avoid large blood vessels, otherwise tumor perfusion will be overestimated.

Wang et al (18) investigated the application of a combination of scalar DTI parameters for the classification of solitary GBM and MET tumors, and achieved an area under receiver operating characteristic (ROC) curve (AUC) of 0.98. However, Wang et al (18) delineated several ROIs both inside and outside the tumor core, which potentially provides a subjectivity that may reduce experimental reproducibility.

The best results of previous studies show classification rates of >90% (18–21); however, the major limitations are that these studies frequently require multiple imaging modalities (19) and subjective selection of peritumoral regions (18,20,21). Moreover, lower classification rates (60–80%) or <0.8 average AUC were reported to distinguish GBM and MET in other previous studies (13,14,16,17,22–25).

As in recent investigations (26,27), we hypothesize that quantitative parameters derived from tumor shape can be used to differentiate GBM from solitary MET, but have derived 3D shape features to more fully describe the tumor morphology. GBMs develop as a diffuse process with preferential infiltration generally by means of white matter tracts, with less common cases growing along the edge of cerebrospinal fluid filled spaces or meninges (28). Consequently, their resultant growth is irregular, and it has been proposed that the shape of the tumor boundary is more likely to be complex (29). In contrast, in METs the proliferation rate is relatively low compared with GBM and the tumor mass is anticipated to expand more homogeneously with cell adhesion being sufficient to maintain a compact spheroidal tumor shape (26,27,30).

To overcome limitations of tumor boundary definitions based on qualitative gray-scale intensities from conventional structural MRI we developed a novel analysis framework that uses quantitative DTI to generate our 3D shape model, from which subsequent tumor classification is provided. This framework is summarized in Figure 1. In particular, we used the DTI Segmentation (D-SEG) technique (31) to provide information regarding the localization and definition of the tumor region of interest, i.e., to create 2D binary masks of the tumor core for both GBM ($N_{GBM} = 30$) and MET ($N_{MET} = 18$), from which the 3D tumor surface morphology could then be derived. Morphological parameters of 3D shape index and curvedness were computed over the whole tumor. In a novel application of the k-medians clustering technique (32) we then derive distinct classes of shape features from the 2D histogram of shape index and curvedness parameters (33). This shape feature extraction method in the 2D shape index and curvedness space is analogous to the D-SEG partition in 2D (p,q) space, and avoids any assumptions of Gaussianity in describing the overall feature distributions. Subsequently we used minimum Redundancy and Maximum Relevance (mRMR) feature selection (34) before tumor classification using Support Vector Machines (SVM) (35). To the best of our knowledge, this represents the first use of 3D shape analysis to quantify and classify tumor morphology from MRI of brain tumors.
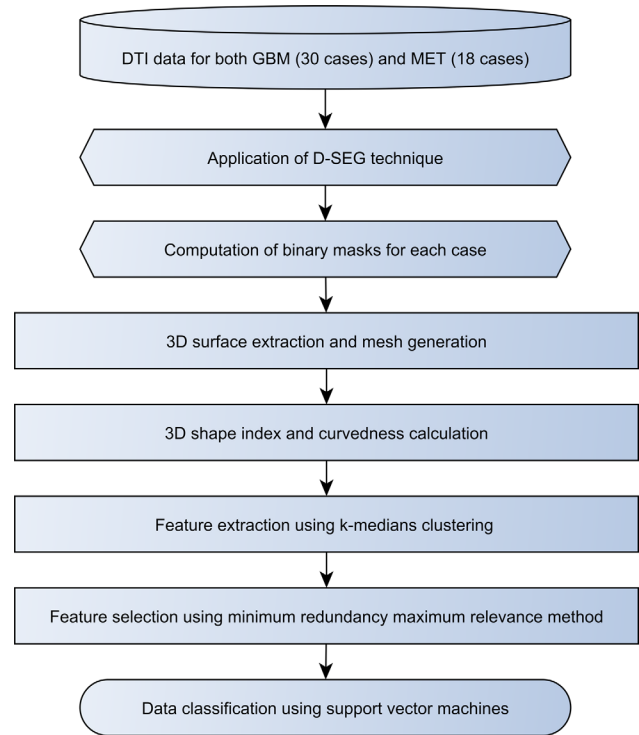

FIG. 1. Flowchart of the 3D morphometric analysis framework.

METHODS

Data Acquisition

Scanner A (2005–2006)

MR imaging data were acquired on a GE Signa LX 1.5 Tesla (T) MRI system (GE Healthcare, Milwaukee, WI) equipped with a maximum field gradient strength of 22 mT/m using a quadrature head coil. Axial DTI datasets were obtained using a single-shot spin echo echo-planar-imaging (EPI) sequence with, two acquisitions without diffusion sensitization (b = 0 s/mm2) and one diffusion-weighted acquisition (b = 1000 s/mm2) in 12 diffusion gradient directions. Whole brain coverage was provided by 50 contiguous slices acquired as two interleaved series of four repeats (slice thickness 2.8 mm with slice gap 2.8 mm, repetition time/echo time (TR/TE) = 8000/88 ms, acquisition matrix = 96 × 96, FOV = 240 mm, and resulted in in-plane resolution of 2.5 × 2.5 mm2).

Scanner B (2008–2010)

MR imaging data were acquired on a GE Signa HD 1.5T MRI system (GE Healthcare, Milwaukee, WI) equipped with 33 mT/m gradients using an 8-channel head coil. Axial DTI datasets were obtained using a similar EPI sequence as aforementioned but with 61 gradient directions. Whole brain coverage was provided by 55 slices (TR/TE = 14150/93.6 ms, acquisition matrix = 96 × 96, field of view [FOV] = 240mm, providing isotropic voxel resolution 2.5 × 2.5 × 2.5 mm^3). Array Spatial Sensitivity Encoding Technique (ASSET) based parallel imaging was applied to accelerate image acquisitions and 10 volumes of $b = 0$ s/mm^2 scans were acquired and averaged.

Patient Data

In agreement with the local regional ethics committee $N_{Total} = 48$ patients were recruited in two blocks between 2005 and 2006 (11 GBM and 9 MET) and 2008–2010 (19 GBM and 9 MET) and retrospectively entered into this study. Patients were not subject to any treatment before radiological examination and had no prior history of surgery, chemotherapy, or radiation therapy. Histopathological analysis of resected tissue confirmed diagnosis of GBM in $N_{GBM} = 30$ patients. For patients with MET ($N_{MET} = 18$), histopathologic analysis revealed 6 cases to have originated from the lung, 2 cases from the breast, 2 from squamous cells, 2 from bowel adenocarcinoma, 1 from melanoma, 1 from renal cancer, 1 neuroendocrine case, 1 from prostate cancer, and 2 from an unknown source.

Feature Extraction

DTI Segmentation

To the best of our knowledge, the majority of previously reported brain tumor MRI segmentation techniques have been applied to conventional structural MRI alone. These segmentations were then applied to quantify diffusion MRI characteristics within segmented ROIs. In contrast, our D-SEG method is applied directly to whole brain DTI acquired across all patient data simultaneously (31), and provides a segmentation of isotropic (p) and anisotropic (q) diffusion characteristics in a 2D (p,q) feature space with minimal observer input. This 2D segmentation is then mapped into the individual's image acquisition space for further analysis. Full details on the D-SEG technique may be found elsewhere (31). In brief, D-SEG applies an unsupervised k-medians clustering algorithm (32), which iteratively segments (p,q) space into $\hat{k}$ nonoverlapping clusters. Our previous study (31) showed that $\hat{k} = 16$ can identify the range of potential tissue compartments present within a brain affected by a tumor, e.g., normal appearing white matter, normal appearing gray matter, cerebrospinal fluid spaces, solid tumor, regional tumor necrosis, tumor-associated cystic regions, perilesional edema, perilesional tumor infiltrations and distant edema. In addition, multiple clusters were used to represent gray and white matter due to heterogeneity of tissue diffusion characteristics throughout normal healthy brain.

The D-SEG technique offers the opportunity to generate a color map of the p and q characteristics for each patient (31). First, T_2-weighted ($b = 0$ s/mm^2) images were histogram normalized and scaled between 0 and 1 on a subject-by-subject basis. Second, median values for each of the 16 cluster centroids for p, q, and T_2-weighted intensity across the patient cohort were ranked (from 1 to 16). Rank scores of T_2-weighting were assigned to the red channel, p to the green channel, and q to the blue channel using a 24-bit RGB color scheme (Figs. 2a,d). Our previous research (31) has shown that clusters 7, 9, 11, 13, 15, and 16 represent a range of diffusion characteristics associated with necrotic and cystic tumor core components and viable or infiltrative tumor in GBM and MET patients as compared to clusters 2, 3, 4, 5, and 6

that represent diffusion in healthy white matter. Regions of extensive edema were excluded. Example D-SEG color maps through an axial slice of a MET case are shown in Figure 2b.

Tumor core ROIs were extracted from the D-SEG segmentation by application of a semiautomated flood-fill method. Seed voxels were manually placed within the tumor core region and flood-filling was used to extract the tumor ROIs from the D-SEG results (Fig. 2c). Example segmentations and tumor core ROIs are shown for GBM and MET cases in Figures 2e–n).

Surface Extraction and Mesh Generation

The standard marching cubes method (36), was applied to the segmented binary mask obtained from D-SEG of the tumor core to generate a triangulated tumor surface mesh with a spatial resolution of 0.375 mm, i.e., triangle side length. The tumor surface represents a sub-voxel isosurface of intensity 0.5 in the binary tumor core map.

3D Shape Descriptors

Shape index (SI) and curvedness (Cv) were derived as 3D shape descriptors from the surface mesh of the tumor core. As there is no global coordinate system for implicitly defined 3D surfaces, the differential geometric features are considered on local Monge form patches where the point of interest on the surface is located at the origin of a local coordinate system (33). For a surface $S \in \mathbb{R}^3$, a surface in Monge form is given by the graph of a smooth function $z = f(x, y)$ with tangent plane, $z = 0$, defined by the properties of unit normal vector n $= (0, 0, 1)$ (see Figure 3a). In general, there are two extreme values (i.e., minimum and maximum) values for the curvature of the surface at the origin, these are termed the principal curvatures, κ_1 and κ_2, and have associated principal tangent directions. The principal curvatures are the eigenvalues of the second fundamental form on the tangent plane and are calculated from the local Hessian matrix, H, where

$$H(f) = \begin{pmatrix} \frac{\partial^2 f}{\partial x^2} & \frac{\partial^2 f}{\partial x \partial y} \\ \frac{\partial^2 f}{\partial y \partial x} & \frac{\partial^2 f}{\partial y^2} \end{pmatrix}. \qquad [1]$$

In this study, we locally approximate the surface using quadratic surface patches of the form

$$f(x, y) = \frac{1}{2} \left(ax^2 + 2bxy + cy^2 \right) \qquad [2]$$

giving the second fundamental form as

$$H = \begin{pmatrix} a & b \\ b & c \end{pmatrix} \qquad [3]$$

with principal curvatures obtained from the solution of the characteristic equation, $H - \kappa I = 0$. This gives principal curvatures as the eigenvalues

$$\kappa_1 = \frac{1}{2} \left(a + c + \sqrt{a^2 + c^2 + 4b^2 - 2ac} \right) \qquad [4]$$
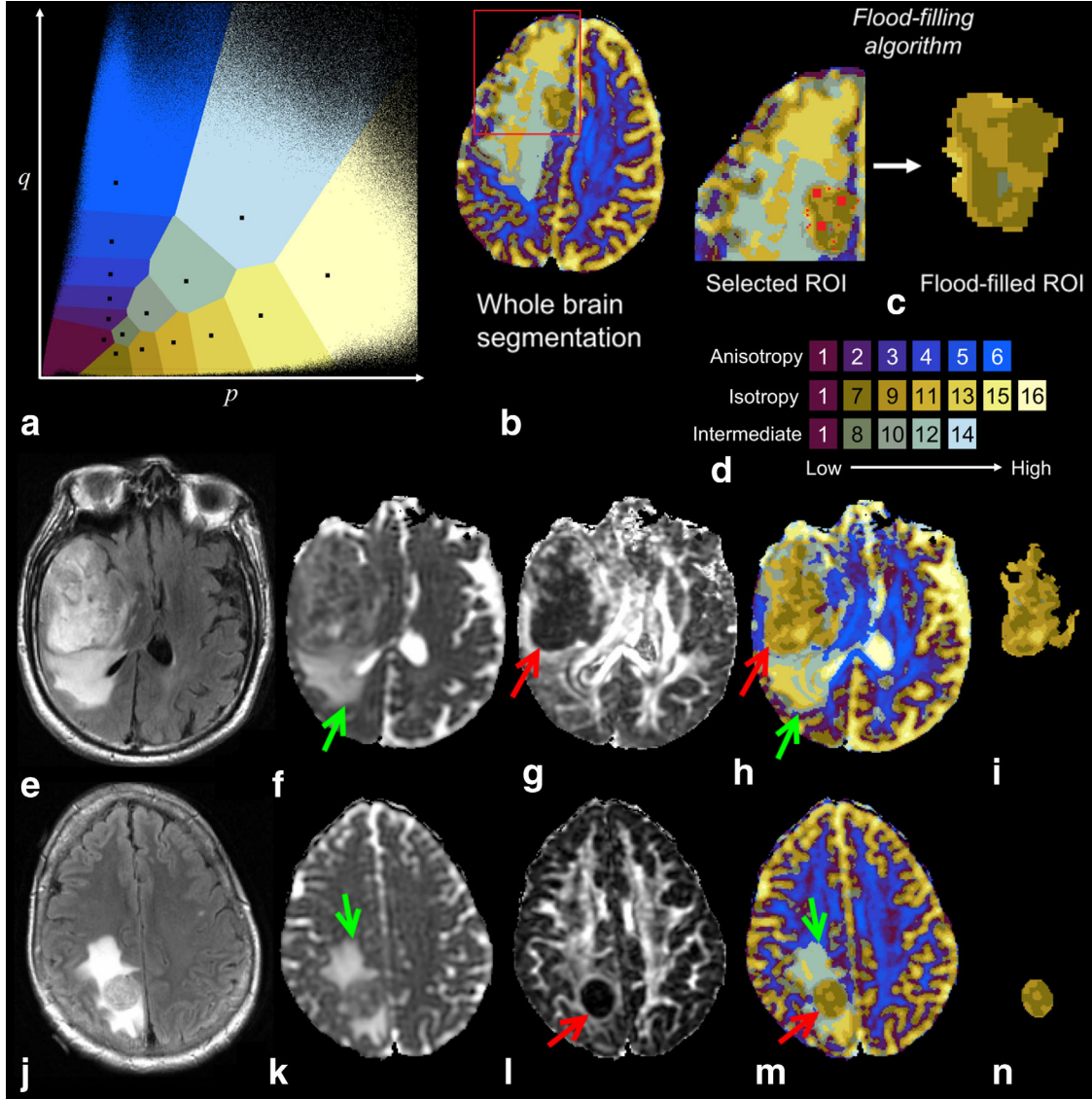
FIG. 2. **a**: D-SEG results in (*p,q*) space represented by a Voronoi plot of the k-medians ($\hat{k} = 16$) segmentation with cluster centroids represented by black dots. **b**: Example whole brain segmentation generated by the D-SEG method. **c**: Schematic for the flood-filling procedure. Multiple seed voxels (colored in red) were required to extract the entire boundary of the tumor core. **d**: The segment number for anisotropic, isotropic and intermediate diffusion patterns, respectively. (**e–i**): A GBM case and (**j–n**): A MET case. Panels (e,j) show FLAIR images, panels (f,k) *p*-maps, panels (g,l) *q*-maps, panels (h,m) whole brain D-SEG, and panels (i,n) the flood-filled tumor core ROI segmentation. Red arrows highlight regions of tumor core with green arrows showing regions of surrounding edema.

$$\kappa_2 = \frac{1}{2}\left(a+c-\sqrt{a^2+c^2+4b^2-2ac}\right). \qquad [5]$$

As all local approximations for which the ratio of the principal curvatures is equal are of the same shape (37), an intuitive notion of shape can be defined in a polar coordinate system of κ_1 and κ_2 (Fig. 3b). Here the angular direction in this polar coordinate system encodes the shape index (SI), and the distance from the origin encodes the sharpness of the shape, known as the curvedness (Cv). Subsequently, SI and Cv can be defined from the two principal curvatures (38). The shape index is given by

$$\begin{aligned}
\mathrm{SI} &= \frac{1}{2} - \frac{1}{\pi}\arctan\frac{\kappa_2+\kappa_1}{\kappa_2-\kappa_1} \\
&= \frac{1}{2} - \frac{1}{\pi}\arctan\left(\frac{-a-c}{\sqrt{a^2+c^2+4b^2-2ac}}\right),
\end{aligned} \qquad [6]$$

in which $\kappa_1 \geq \kappa_2$, and $\mathrm{SI} \in [0,1]$. In addition, the curvedness is defined as the length of the shape vector

$$\mathrm{Cv} = \sqrt{\frac{\kappa_1^2+\kappa_2^2}{2}} = \sqrt{\frac{a^2+c^2+2b^2}{2}}. \qquad [7]$$

The scaling factor 2 is used to ensure that the curvedness equals 1 in the case of unit sphere (38). Then the curvedness has been normalized so that $\mathrm{Cv} \in [0,1]$.
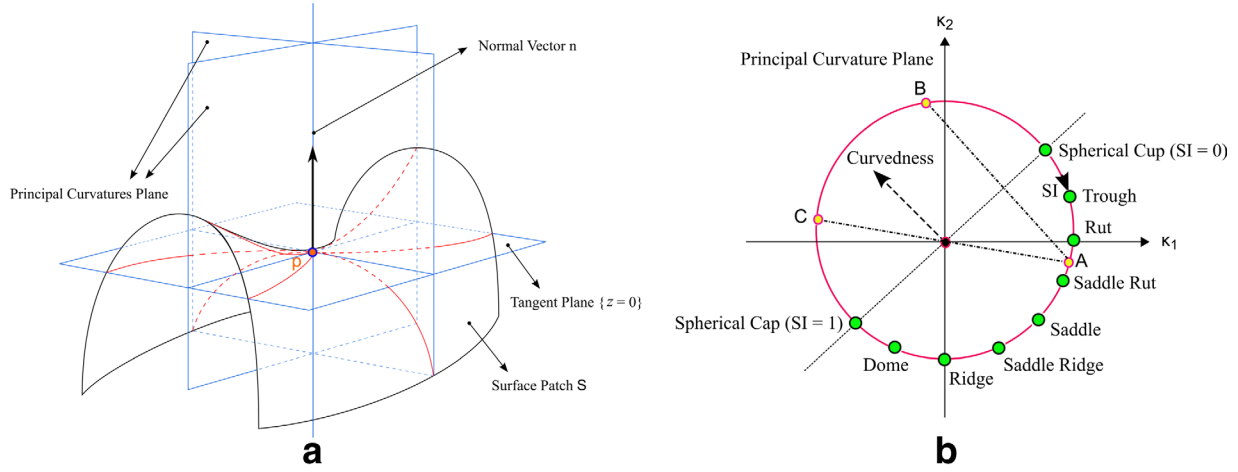
FIG. 3. **a**: An illustration of the principal curvatures. A saddle surface patch is shown expressed by $f(x, y) = x^2$-y^2. When the normal plane perpendicular to the tangent plane is rotated around the normal vector at the origin, p, the resultant curves defined on the surface patch have curvatures known as the normal curvatures. The maximum and minimum of these curvatures are the principal curvatures, κ_1 and κ_2. **b**: The polar coordinate system of the principal curvature (κ_1, κ_2) plane, in which the shape index and the curvedness are defined. The antipodal points **A** and **C** denote opposite shapes, e.g., spherical cup and cap. Points **A** and **B** are related by reflection such that they represent similar features under 90-degree-rotation.

Histogram Analysis and Clustering

Our previous research using 2D shape analysis extracted global shape features and calculated the first and second order statistics assuming the 2D shape features are normally distributed (27). However, assumptions of normality are invalid for our local 3D shape features. Figure 4 shows

FIG. 4. **a,d**: Color coded surface shape index maps for a GBM (a) and a MET (d) case. **b,e**: Color coded curvedness maps for the same GBM and (b) MET (e) cases. **c,f**: Example 2D histograms in (SI,Cv) space for the GBM and the MET case, respectively.

example surface meshes of a typical GBM and MET case colored by shape index (Figs. 4a,d) and curvedness (Figs. 4b,e) and the resultant 2D histograms in SI (horizontal axis) and Cv (vertical axis) space for the GBM and the MET case, respectively (Figs. 4c,f). This representation of (SI,Cv) space shows SI to follow a multimodal distribution and also that the Cv distribution is highly skewed. Consequently the use of parametric statistical analysis such as quantification of mean and standard deviation is insufficient for describing the behavior of 3D shape parameters.

To overcome this limitation, we propose an analogous technique to D-SEG to analyze the 2D histogram of 3D shape features computed on the surface mesh. In particular, we propose a k-medians clustering to partition the 2D histogram. The percentage contribution of each cluster of each patient was calculated to provide features for further classification, that is

$$F(i, m) = \frac{\sum_{j}^{Q_i} c(h_{ij}, m)}{Q_i} \times 100;$$

$$\text{where } c(h_{ij}, m) = \begin{cases} 1 \text{ if } c(h_{ij}) = m \\ 0 \text{ if } c(h_{ij}) \neq m, \end{cases} \quad [8]$$

and $i \in \{1, 2, \ldots, N_{Total}\}$ represents the set of patients and $m = \{1, 2, \ldots, k\}$ represents the set of clusters. In addition, Q_i is the total number of surface patches for the i-th patient and $c(h_{ij})$ stores clustered labels for each of the j surface patches for the i-th patient. One "simple rule of thumb" for choosing k for k-medians clustering is that $k \approx \sqrt{N_{Total}/2}$ (39). In addition, to avoid overfitting the classifier previous research has advised a sample per feature ratio (SFR) of at least 5 to 10 (40). Therefore, we fixed $k = 6$ for our k-medians clustering with an SFR = 8.

Statistical Analysis

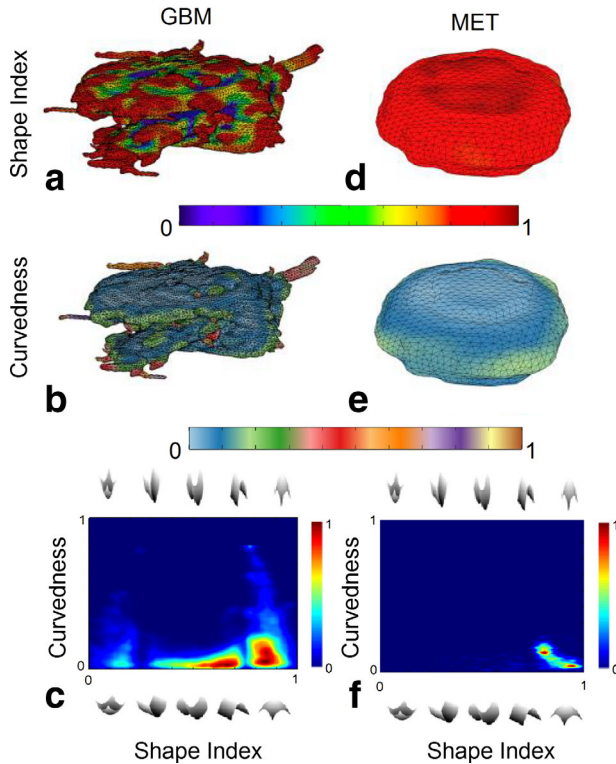Percentage contributions obtained from the study population ($N_{Total} = 48$) were compared between GBMs and

solitary METs using the nonparametric Wilcoxon Rank-Sum Test after Bonferroni correction for the number of extracted features (i.e., $k = 6$ provides a significance threshold of $P < 0.05/6 = 8.33 \times 10^{-3}$). The P-values obtained by the statistical analysis correspond to the features identified by the feature selection scheme (below).

Classification

Pattern Classification Using Nonlinear SVM

SVM provide a powerful technique for binary classification (35). SVM predictions depend on a subset of training data (i.e., the support vectors), and find the hyperplane with largest margin between the two classes (41). This is obtained by solving the following optimization problem,

$$\min_{w,b,\zeta} \frac{1}{2} w^T w + \rho \sum_{i=1}^{l} \zeta_i$$
$$\text{subject to } y_i \left(w^T \varPhi(x_i) + b \right) \geq 1 - \zeta_i \text{ and } \zeta_i \geq 0 \quad [9]$$

in which (x_i, y_i), $i = 1, 2, \ldots, l$ is the instance-label pairs of the given training dataset (42). Here $\langle w, x \rangle + b = 0$ defines the hyperplane for $b \in \mathbb{R}$ is real. Furthermore, L_1-norm based formulation of the soft margins was applied by adding slack variables ζ_i and a penalty parameter ρ, which is known as the box constraint for the soft margin. In addition, $K(x_i, x_j) \equiv \varPhi(x_i)^T \varPhi(x_j)$, is called the kernel function. In this study, we used a nonlinear Gaussian Radial Basis Function (RBF) kernel $K(x_i, x_j) = \exp\left(-\gamma \|x_i - x_j\|^2\right)$ with scaling-factor, $\gamma > 0$, to map feature vectors into a nonlinear feature space where an optimal hyperplane was constructed to separate the GBM and MET classes. The two parameters of the SVM with a RBF kernel (i.e., ρ and γ) were optimized using cross-validation with a grid search scheme (42). In this study we formed a 10×10 "grid" using $\rho = 2^{-5}, 2^{-3}, 2^{-1}, \ldots, 2^{11}, 2^{13}, 2^{15}$ and $\gamma = 2^{-5}, 2^{-3}, 2^{-1}, \ldots, 2^{11}, 2^{13}, 2^{15}$. The grid search results of SVM are shown in Figure 5a, and indicate that $\rho = 2^4$ and $\gamma = 2^{10}$ reached the maximum accuracy and minimum balanced error rate. These parameters were used in the study.

Performance Assessment and Feature Searching

Classification performance of our 3D shape analysis framework was evaluated by: (i) Leave-One-Out (LOO) cross validation at the patient level, which provides an unbiased predictor and capable of creating sufficient training data for studies with small sample size (43); (ii) the cross validated classification accuracy, sensitivity, specificity, and AUC; and (iii) the balanced error rate (BER) (44). Overall, we advocated the BER metric as the main criterion to evaluate classification performance because of the unequal numbers of GBM ($N_{GBM} = 30$) and MET ($N_{MET} = 18$) samples. To avoid possible bias in the feature extraction process, the unsupervised k-medians clustering was embedded into the LOO cross validation. For example, for each fold of the cross validation, k-medians clustering on 47 samples was performed, and clustering labels of the omitted case were predicted based on the calculated centroids. Clustering stability (CS) (45) was also calculated. This was defined as the sum of percentage difference between k-medians clusters across all 48 samples and k-medians results of each of the LOO cross validation, such that

$$CS = \frac{\sum_i^{N_{Total}} \sum_j^{Q_i} c(f_{ij}, g_{ij})}{N_{Total} \times Q_i} \times 100;$$
$$\text{where } c(f_{ij}, g_{ij}) = \begin{cases} 1 \text{ if } c(f_{ij}) = c(g_{ij}) \\ 0 \text{ if } c(f_{ij}) \neq c(g_{ij}), \end{cases} \quad [10]$$

in which $c(g_{ij})$ stores clustered labels for each of the j surface patches for the i-th patient using all $N_{Total} = 48$ samples, and $c(f_{ij})$ represents results of i-th fold of LOO cross validation. Therefore, $CS \in [0, 1]$, and as $CS \rightarrow 1$, the k-medians clustering results are more stable for each LOO fold.

Feature selection is a crucial step for any pattern recognition task, and the aim is to discover a compact and informative representation of the obtained data without substantial loss in discriminative power (46). In this study, we used a mutual information based mRMR method for feature selection (34). The only parameter required for the mRMR method is the number of selected features denoted here as $|Q| = \{1,2,3\}$. The feature selection step identified the feature set with the lowest cross-validated BER. These classification results were compared with those obtained using the 2D shape information in our previous study (27).

RESULTS

Figures 2e–i and 2j–n shows typical GBM and MET cases, respectively. The tumor core was clearly observed in the q maps (as areas of low anisotropic diffusion indicated by red arrows in Figures 2g,l), and the surrounding edema in p maps (as areas of high isotropic diffusion indicated by green arrows in Figures 2f,k). Figures 2h,m illustrate the whole brain segmentations generated by D-SEG. By applying the semiautomated flood-fill algorithm, tumor ROIs are segmented as shown in Figures 2i,n. These were used as binary masks to create surface meshes and extract 3D shape features. In general, GBM cases have more heterogeneous tumor ROI boundaries. For example, Figures 2e–i shows a GBM with potentially infiltrative features extending into normal appearing white matter. In contrast, Figures 2j–n shows a MET in the right parietal lobe area that the tumor core is much more localized and spherical.

Figure 4 shows color coded shape index and curvedness values mapped onto tumor core ROI surface meshes for the tumor cases shown in Figure 2. Figures 4a,b show shape index and curvedness results for the GBM case and Figures 4d,e show the MET case. SI and Cv are more uniform in this MET case compared with the GBM case. The 2D histogram of (SI,Cv) space for the two cases are shown in Figures 4c,f. These histograms show that the distribution of SI and Cv values are more heterogeneous for the GBM case than for the MET.
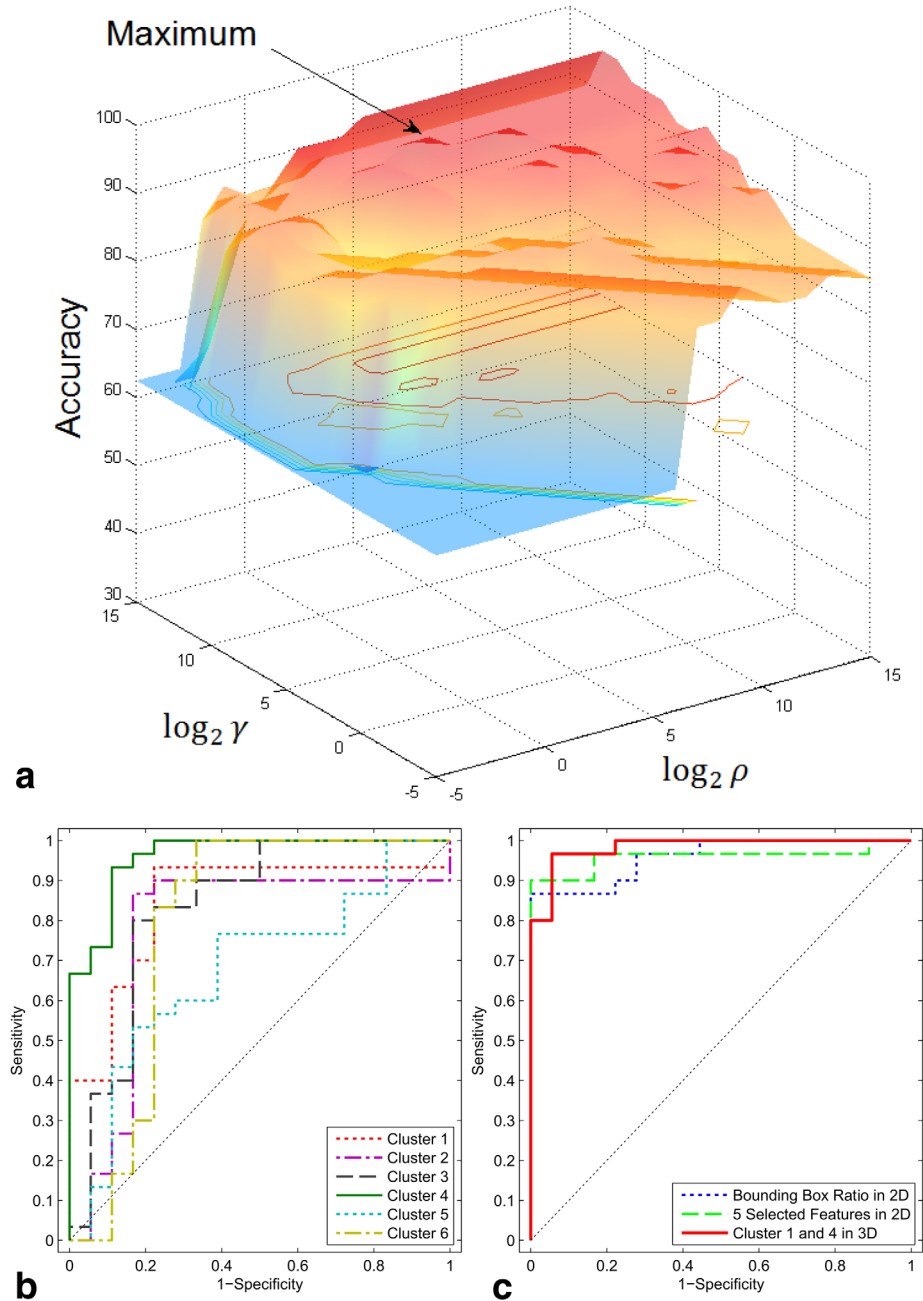
FIG. 5. **a**: Plot of the grid search performed to optimize the box constraint, ρ, and scaling factor, γ, for application of the Gaussian Radial Basis Function kernel of the SVM classifier. The maximum accuracy achieved by the grid search is highlighted by the arrow. **b**: Comparison of the ROC analysis using each single cluster. **c**: Comparison of the ROC analysis using a single 2D bounding box ratio, 5 selected 2D shape features, and cluster 1 and 4 in 3D.

Figure 6a demonstrates the result of k-medians clustering applied to the full 48 patient dataset to produce a Voronoi plot partitioned into six segments (cluster 1 to 6). Figure 6b shows the normalized frequency histogram in (SI,Cv) space for all GBM patients ($N_{GBM} = 30$), and Figure 6c shows the normalized frequency histogram in (SI,Cv) space for all MET patients ($N_{MET} = 18$). In the LOO cross validation, k-medians clustering was applied to each fold for 47 patient cases, to avoid potential bias in prediction of the clustering labels. Clustering stability was calculated as 99.7%. Percentage contribution of each cluster for each patient was then calculated as features for further classification. These features provide an assessment of the heterogeneity of the 3D shape parameters within the 2D (SI,Cv) space.

Figure 7 shows boxplots of percentage contribution of each cluster for each patient and visualize the significant differences between GBM and MET cases shown in Table 1. The greatest significant difference between tumor types was found in cluster 1 and 4, with only clusters 3 and 5 providing no significant difference between GBM and MET cases. SVM classification between the GBM and MET cases using the percentage contribution for each cluster separately (Table 2) revealed cluster 1 (BER = 0.14) and cluster 4 (BER = 0.09) to perform the best with the worst performance obtained using cluster 3 or 5 (BER > 0.2). By consideration of the (SI,Cv) coordinates of cluster 1 and 4 in Figure 3b, it is apparent that cluster 1 and 4 represent convex (spherical cap) and concave
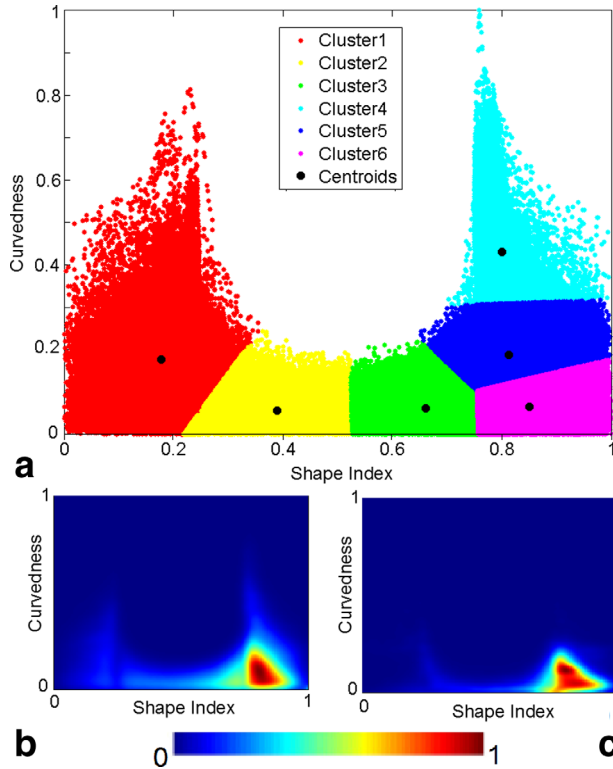
FIG. 6. **a**: Voronoi plot of the k-medians ($k=6$) clustering results performed on all patient data ($N_{GBM}=30$, $N_{MET}=18$) in the 2D (SI,Cv) space. **b,c**: 2D histograms in (SI,Cv) space for all the GBM cases ($N_{GBM}=30$) and all the MET cases ($N_{MET}=18$), respectively.

(spherical cup) shapes, respectively, with greater percentage contribution of both clusters in GBM than MET cases. These findings also correlate with the 2D histograms of all the GBM and all the MET cases (Figure 6b versus Figure 6c), in which GBM cases always present data points in cluster 1 and 4 regions of the (SI,Cv) space while MET cases are lack of data points in these regions. In contrast, the other clusters are overlapping in the (SI,Cv) space for both GBM and MET cases.

ROC analysis also showed that cluster 4 obtained the highest AUC (0.961), which is significantly different ($P<0.05$ according to the ROC comparison method described in Hanley and McNeil and Gur et al) (47,48) from the AUC results obtained using other features alone (Table 2 and Figure 5b). We obtained BER of 0.09, 0.04, and 0.06 by setting the number of selected features $|Q|=1$, 2, and 3 using the mRMR method. The selected features were cluster 4, clusters 1 and 4, and clusters 1, 3, and 4 for $|Q|=1$, 2, and 3, respectively. $|Q|=2$ provided the lowest BER (BER $=0.04$, see Table 3). This cluster combination (clusters 1 and 4) performs better than our previously published 2D shape feature selection method using bounding box ratio (BER $=0.1$) (27) and five selected 2D shape features (BER $=0.08$) (27) applied to the same D-SEG tumor ROIs. An improved AUC was also obtained (0.959 for 2D versus 0.983 for 3D) suggesting that classification performance using clustered 3D shape features is improved compared with using 2D morphometric features on the same data (Table 3 and Figure 5c).

Our 3D shape analysis framework was implemented in *Matlab* (Matlab 2013a, Mathworks, Natick, MA) on a 64-bit computer having *Intel Core 2 Duo E6850* processor (3.00 GHz) and 4GB of memory. The feature extraction procedure took 210 s processing time and SVM classification required an additional 89 s to obtain the final results.

DISCUSSION

The objective of this study was to develop a 3D morphological model to classify GBMs from solitary METs. Results of this study provide compelling evidence that our 3D shape analysis is capable of distinguishing between these brain tumor types providing improved results compared with classification based on 2D shape features.

Conventional structural MRI can provide useful information to aid delineation of brain tumor boundaries; however, if these are not based on quantitative MRI scans, the boundaries will be influenced by intensity nonuniformity and different acquisition parameters (e.g., TE and TR). Moreover, different clinical MRI modalities (e.g., T_2 or T_1 postcontrast) show very different tissue characteristics and hence different tumor boundaries. In contrast, D-SEG provides a quantitative generation of ROI boundaries (Figs. 2i,n) based on diffusion characteristics (i.e., p and q). In so doing, D-SEG can identify subtle changes of tumor shape due to disruption of brain tissue microstructure caused by tumor growth and infiltration.

By performing histogram analysis on extracted local three-dimensional shape parameters, i.e., SI and Cv (Figs. 3, 4a,b), a full quantitative description of individual tumor morphology is obtained. SI shows a multimodal distribution and the Cv distribution is highly skewed (Figs. 4c,f); therefore, mean and standard deviations derived from these parameters are insufficient to fully describe the shape of individual tumors. Consequently, we used the unsupervised k-medians method to partition
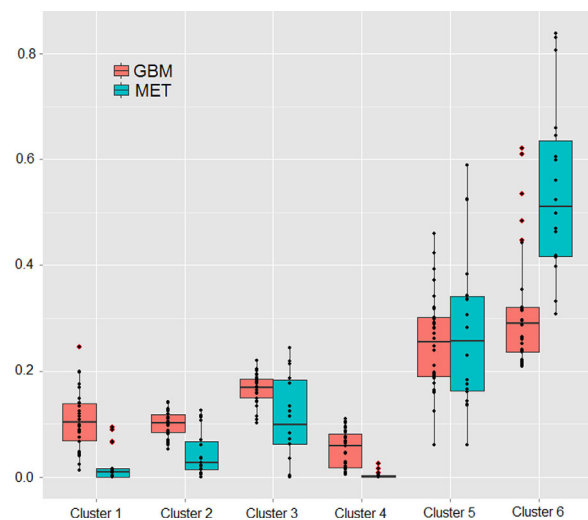

FIG. 7. Boxplot showing the percentage contribution to each of the six clusters for $N_{GBM}=30$ (red) and $N_{MET}=18$ (cyan) cases. Upper and lower quartiles and medians are marked.

Table 1

Wilcoxon Rank-Sum Test Results between GBM and MET Groups for Percentage Contribution of Clusters[a]

	Wilcoxon rank-sum test ($P < 8.33E\text{-}03$ by Bonferroni correction)					
	Cluster 1	Cluster 2	Cluster 3	Cluster 4	Cluster 5	Cluster 6
P-values	1.24E-06	1.57E-04	1.75E-02	6.61E-08	9.58E-01	2.47E-06

[a]After Bonferroni correction, the significance threshold was $P < 8.33 \times 10^{-3}$.

the 2D SI and Cv histogram space into six clusters using a moderate SFR value to avoid overfitting (Fig. 6a). Feature selection using mutual information based mRMR method showed that the combination of cluster 1 and 4 achieved the best classification performance. Figures 6b,c show that the average 2D histograms of the GBM and MET cases are dense over cluster 3, 5, and 6; however, the GBM histogram extends into clusters 1, 2 and 4. Visual inspection of the 2D histograms of 48 patient cases showed that a small number of MET cases presented contributions to clusters 1 and 4, while all GBM cases included cluster 1 and 4 components. This observation is in correspondence with our statistical analysis which identified clusters 1 and 4 as the most significantly different features for distinguishing GBMs from solitary METs (Table 1).

According to the polar coordinates of SI and Cv (Fig. 3b), cluster 1 and 4 represent spherical cap and cup shapes, respectively. Both GBM and MET cases exhibit large amounts of spherical cap components; however, MET consist of spherical caps with much lower curvedness, which are mainly represented by cluster 5 and 6. Conversely, GBM also contains "spiky" cap shapes due to infiltrative characteristics, which are identified in our analysis by large proportions of cluster 4. In addition, GBM also possesses more concave shapes while MET is more likely to have convex surfaces. Consequently, GBM cases dominate the cluster 1 region. Interestingly, cluster 6 can be used as a distinguishable feature (p = 2.47E−06). Cluster 6 includes spherical cap and dome regions with large variation in curvedness. The difference between GBM and MET cases may be attributed to the greater variance in the GBM surface, whereas the MET cases are more compact. Overall, our selected features (i.e., clusters 1 and 4) not only produced the best classification performance but was also consistent with the pathological characteristics of the two tumor types, i.e., heterogeneity for GBMs and homogeneity for solitary METs.

Our tumor classification based on clusters 1 and 4 provided an accuracy of 95.8%, sensitivity of 94.4%, speci-

ficity of 96.7%, AUC of 0.983, and BER of 0.04. Previous studies using advanced MRI techniques have provided similar classification quality. By acquiring both MRS and DSC-MRI perfusion data on solitary GBM or MET, Tsolaki et al (19) obtained the lowest published BER of 0.02 by computing the metabolic ratio of N-acetyl aspartate and Creatine (NAA/Cr) from peritumoral area. However, MRS data acquisition requires subjective selection of MRS voxels from which to obtain data, careful planning to avoid poor water suppression and signal contamination by scalp lipids that would distort the spectroscopy data. In addition, Tsolaki et al (19) demonstrated that relative cerebral blood volume (rCBV) of the peritumoral region provided high classification accuracy (97% ± 3% using naïve Bayes and 89% ± 5% using k-nearest neighbors classifiers). To achieve their classification, Tsolaki et al (19) manually placed user-defined ROIs of variable size (from 25 mm^2 to 62 mm^2) and number (between 3 and 10) in both the intratumoral and peritumoral areas to extract areas with hyperperfusion. Svolos et al (21) used a similar ROI based technique to calculate rCBV, apparent diffusion coefficient (ADC) and fractional anisotropy (FA) and used these to obtain classification accuracies of 75% ± 2% for intratumoral and 96% ± 2% for peritumoral ROIs. These ROI based procedures are highly user-dependent and elevated rCBV values from large vessels near or within the tumor area potentially represents a confounding factor, which could overestimate perfusion within infiltrated oedema. In contrast, our D-SEG maps are computed from a single imaging modality across the entire brain DTI.

Wang et al (18) and Wang et al (49) have investigated characteristics of scalar DTI parameters [i.e., ADC, FA, linear anisotropy (CL), and planar anisotropy (CP)] for semiautomatically segmented regions from FLAIR and Gadolinium contrast enhanced T1-weighted images of solitary GBM and MET patients. The most promising classification was with a model based on ADC, FA, and CP of the contrast enhancing region, which achieved an AUC of 0.98 whereas a single scalar parameter provided

Table 2

Quantitative classification of percentage contribution for each single cluster

	Leave-One-Out Cross-Validation Results Using SVM				
Features	Accuracy	Sensitivity	Specificity	AUC	BER
Cluster 1	87.50	77.78	93.33	0.844	0.14
Cluster 2	83.33	77.78	86.67	0.772	0.18
Cluster 3	81.25	50	100	0.832	0.25
Cluster 4	91.67	88.89	93.33	0.961	0.09
Cluster 5	68.75	16.67	100	0.678	0.42
Cluster 6	87.50	66.67	100	0.789	0.17

AUC = area under ROC curve; BER = balanced error rate.

Table 3
Classification Results for Percentage Contribution of Cluster 1 and 4[a]

	Leave-One-Out Cross-Validation results using SVM						
Features	Predicted group membership		Accuracy	Sensitivity	Specificity	AUC	BER
Bounding box ratio in 2D	GBM	MET	87.5	100	80	0.959	0.1
GBM	24	6					
MET	0	18					
5 Selected features in 2D	GBM	MET	91.67	94.44	90	0.959	0.08
GBM	27	3					
MET	1	17					
Cluster 1 and 4 in 3D	GBM	MET	95.83	94.44	96.67	0.983	0.04
GBM	29	1					
MET	1	17					

[a]Results are compared with previously published 2D shape feature classification techniques using a single 2D bounding box ratio or 5 selected 2D shape features.
AUC = area under ROC curve; BER = balanced error rate.

a maximum AUC of 0.9 for FA or CL (18). In a larger study, a classification model based on fractional anisotropy and mean diffusivity achieved a lower AUC of 0.86, but when used as a decision support tool helped improve diagnostic accuracy of expert neuroradiologists to an AUC of up to 0.96 (49). We obtain an AUC of 0.98 with our 3D shape analysis using two shape parameters (clusters 1 and 4) and an AUC of 0.96 using only one 3D shape parameter (cluster 4), suggesting our shape parameters maybe more intrinsically related to the two tumor types. Furthermore, the shape parameters can be determined from DTI without additional information from other imaging modalities. Nevertheless our results require validation with larger patient cohorts.

In our previous classification study that used 2D shape information to discriminate between solitary GBM and MET cases (27), sixty-one 2D shape features were extracted from D-SEG data and followed by a feature selection step five features were selected for further classification. However, the inclusion of greater numbers of features increases the possibility of overfitting the classifier. In this study, we used the SFR criterion to assess the level of overfitting and our technique identified two features (clusters 1 and 4) that achieved the best classification performance with an SFR of 24. In contrast, our 2D analysis used five selected features with an SFR of 9.6. Consequently, the results obtained in this study are less likely to be a result of classifier overfitting. ROC curves comparison showed that the AUC obtained by five selected features in 2D and Cluster 1 and 4 in 3D shape analysis were not significantly different; however, in this study, we advocate the BER as a better criterion of classification performance because of our unbalanced dataset. Further support for the use of the 3D shape features in classification is provided by the improved overall performance compared with the previous 2D shape feature study (Table 3).

There are limitations of the current work. First, we used the semiautomated flood-fill procedure to extract the tumor core ROIs after segmentation of the DTI data by D-SEG. However, the tumor core extraction was performed by a single rater and could be extended to multiple raters on common agreement of which specific clusters in the D-SEG color maps are designated as tumor; hence, the method should provide high reproducibility for definition of complex tumor shapes. Nevertheless, future technical improvement would include a fully automated segmentation method to provide minimal subjectivity in our 3D shape analysis framework. Second, the D-SEG method provides an objective and unsupervised segmentation of brain and tumor tissue into classes of similar water diffusion characteristics, but the clusters are associated with particular tissue types as opposed to being specific to defined histological and anatomical classes. In a previous study (50), we demonstrated that D-SEG clusters within brain tumors are strongly associated with boundaries observed on conventional structural MRI (i.e., clinical T_2-weighted FLAIR and T_1-weighted gadolinium-enhanced MR images). Visual inspection by our Consultant Neurosurgeon (TJ) with over 10 years of experience enabled 2D flood-filled regions representing the tumor core to be extracted from axial slices of D-SEG maps. Tumor ROIs included necrotic and/or cystic core and a surrounding region considered to be viable and/or infiltrative tumor. Extensive regions of edema were excluded. The derived boundary represents the complexity of the interface between tumor tissue and normal brain and is produced objectively and reproducibly by the D-SEG method. However, the boundary does not represent a specific level of tumor infiltration for GBM, and further work is needed to assess this. Third, our retrospective study only had access to solitary GBM cases. Nevertheless, our framework could be applied to multifocal GBM cases by extracting shape index and curvedness information for each lesion separately. Moreover, in this study, we have fixed several parameters in our framework, e.g., $k = 6$ in the k-medians clustering and the spatial resolution of the triangulated tumor surface. We envisage that future assessment of the robustness of our 3D shape analysis framework will include parameter perturbation; however, this should ideally be performed over larger cohorts that include multicenter and multiscanner data.

CONCLUSIONS

We have shown how a 3D morphometric analysis framework can be applied to distinguish GBMs from solitary

METs. The combination of D-SEG applied to DTI data to derive the tumor shape and the 2D histogram analysis of 3D shape parameters provides quantitative parameterization of tumor shape with minimal observer subjectivity. This method can be applied to other tumor and non-tumorous lesions, with potential for classification of disease type and assessment of growth or regression with treatment. We also envisage that the distinct 3D morphological appearance of GBMs and METs provide a new visualization tool for neuroradiologists while also giving improved tumor classification accuracy.

REFERENCES

1. Giese A, Westphal M. Treatment of malignant glioma: a problem beyond the margins of resection. J Cancer Res Clin Oncol 2001;127:217–225.
2. Soffietti R, Ruda R, Mutani R. Management of brain metastases. J Neurol 2002;249:1357–1369.
3. Johnson DR, Ma DJ, Buckner JC, Hammack JE. Conditional probability of long-term survival in glioblastoma: a population-based analysis. Cancer 2012;118:5608–5613.
4. Andrews DW, Scott CB, Sperduto PW, et al. Whole brain radiation therapy with or without stereotactic radiosurgery boost for patients with one to three brain metastases: phase III results of the RTOG 9508 randomised trial. Lancet 2004;363:1665–1672.
5. Rades D, Dziggel L, Haatanen T, Veninga T, Lohynska R, Dunst J, Schild SE. Scoring systems to estimate intracerebral control and survival rates of patients irradiated for brain metastases. Int J Radiat Oncol 2011;80:1122–1127.
6. Tsuchiya K, Fujikawa A, Nakajima M, Honya K. Differentiation between solitary brain metastasis and high-grade glioma by diffusion tensor imaging. Br J Radiol 2005;78:533–537.
7. Law M, Cha S, Knopp EA, Johnson G, Arnett J, Litt AW. High-grade gliomas and solitary metastases: differentiation by using perfusion and proton spectroscopic MR imaging. Radiology 2002;222:715–721.
8. Roy PA, Tibbs PA, Walsh JW, Dempsey RJ, Maruyama Y, Kryscio RJ, Markesbery WR, Macdonald JS, Young B. A randomized trial of surgery in the treatment of single metastases to the brain. N Engl J Med 1990;322:494–500.
9. Nussbaum E, Djalilian H, Cho K, Hall W. Brain metastases: histology, multiplicity, surgery, and survival. Cancer 1996;78:1781–1788.
10. Cha S, Lupo JM, Chen M-H, Lamborn KR, McDermott MW, Berger MS, Nelson SJ, Dillon WP. Differentiation of glioblastoma multiforme and single brain metastasis by peak height and percentage of signal intensity recovery derived from dynamic susceptibility-weighted contrast-enhanced perfusion MR imaging. AJNR Am J Neuroradiol 2007;28:1078–1084.
11. Campos S, Davey P, Hird A, et al. Brain metastasis from an unknown primary, or primary brain tumour? A diagnostic dilemma. Curr Oncol 2009;16:62–66.
12. Schiff D. Single brain metastasis. Curr Treat Options Neurol 2001;3:89–99.
13. Opstad KS, Murphy MM, Wilkins PR, Bell BA, Griffiths JR, Howe FA. Differentiation of metastases from high-grade gliomas using short echo time 1H spectroscopy. J Magn Reson Imaging 2004;20:187–192.
14. Crisi G, Orsingher L, Filice S. Lipid and macromolecules quantitation in differentiating glioblastoma from solitary metastasis: a short-echo time single-voxel magnetic resonance spectroscopy study at 3 T. J Comput Assist Tomogr 2013;37:265–271.
15. Bulakbasi N, Kocaoglu M, Farzaliyev A, Tayfun C, Ucoz T, Somuncu I. Assessment of diagnostic accuracy of perfusion MR imaging in primary and metastatic solitary malignant brain tumors. AJNR Am J Neuroradiol 2005;26:2187–2199.
16. Byrnes TJD, Barrick TR, Bell BA, Clark CA. Diffusion tensor imaging discriminates between glioblastoma and cerebral metastases in vivo. NMR Biomed 2011;24:54–60.
17. Georgiadis P, Cavouras D, Kalatzis I, Glotsos D, Athanasiadis E, Kostopoulos S, Sifaki K, Malamas M, Nikiforidis G, Solomou E. Enhancing the discrimination accuracy between metastases, gliomas and meningiomas on brain MRI by volumetric textural features and ensemble pattern recognition methods. Magn Reson Imaging 2009;27:120–130.
18. Wang S, Kim S, Chawla S, Wolf RL, Zhang W-G, O'Rourke DM, Judy KD, Melhem ER, Poptani H. Differentiation between glioblastomas and solitary brain metastasis using diffusion tensor imaging. Neuroimage 2009;44:653–660.
19. Tsolaki E, Svolos P, Kousi E, Kapsalaki E, Fountas K, Theodorou K, Tsougos I. Automated differentiation of glioblastomas from intracranial metastases using 3T MR spectroscopic and perfusion data. Int J Comput Assist Radiol Surg 2013;8:751–761.
20. Server A, Orheim TED, Graff BA, Josefsen R, Kumar T, Nakstad PH. Diagnostic examination performance by using microvascular leakage, cerebral blood volume, and blood flow derived from 3-T dynamic susceptibility-weighted contrast-enhanced perfusion MR imaging in the differentiation of glioblastoma multiforme and brain me. Neuroradiology 2011;53:319–330.
21. Svolos P, Tsolaki E, Kapsalaki E, Theodorou K, Fountas K, Fezoulidis I, Tsougos I. Investigating brain tumor differentiation with diffusion and perfusion metrics at 3T MRI using pattern recognition techniques. Magn Reson Imaging 2013;31:1567–1577.
22. Devos A, Lukas L, Suykens JAK, et al. Classification of brain tumours using short echo time 1H MR spectra. J Magn Reson 2004;170:164–175.
23. Chen XZ, Yin XM, Ai L, Chen Q, Li SW, Dai JP. Differentiation between brain glioblastoma multiforme and solitary metastasis: qualitative and quantitative analysis based on routine MR imaging. AJNR. AJNR Am J Neuroradiol 2012;33:1907–12.
24. García-Gómez JM, Luts J, Julià-Sapé M, et al. Multiproject-multicenter evaluation of automatic brain tumor classification by magnetic resonance spectroscopy. MAGMA 2009;22:5–18.
25. Server A, Kulle B, Maehlen J, Josefsen R, Schellhorn T, Kumar T, Langberg CW, Nakstad PH. Quantitative apparent diffusion coefficients in the characterization of brain tumors and associated peritumoral edema. Acta Radiol 2009;50:682–689.
26. Blanchet L, Krooshof PWT, Postma GJ, Idema AJ, Goraj B, Heerschap A, Buydens LMC. Discrimination between metastasis and glioblastoma multiforme based on morphometric analysis of MR images. AJNR Am J Neuroradiol 2011;32:67–73.
27. Yang G, Jones TL, Barrick TR, Howe FA. Discrimination between glioblastoma multiforme and solitary metastasis using morphological features derived from the p:q tensor decomposition of diffusion tensor imaging. NMR Biomed 2014;27:1103–1111.
28. Claes A, Idema A, Wesseling P. Diffuse glioma growth: a guerilla war. Acta Neuropathol 2007;114:443–458.
29. Kim Y, Lawler S, Nowicki MO, Chiocca EA, Friedman A. A mathematical model for pattern formation of glioma cells outside the tumor spheroid core. J Theor Biol 2009;260:359–371.
30. Frieboes HB, Zheng X, Sun C-H, Tromberg B, Gatenby R, Cristini V. An integrated computational/experimental model of tumor invasion. Cancer Res 2006;66:1597–1604.
31. Jones TL, Byrnes TJ, Yang G, Howe FA, Bell BA, Barrick TR. Brain tumor classification using the diffusion tensor image segmentation (D-SEG) technique. Neuro Oncol 2014;17:466–476.
32. Bradley PS, Mangasarian OL, Street WN. Clustering via concave minimization. In: Mozer MC, Jordan MI, Petsche T, editors. Advances in neural information processing systems. Cambridge: The MIT Press; 1996. p 368–374.
33. Abbena E, Salamon S, Gray A. Modern differential geometry of curves and surfaces with mathematica. 2nd ed. Boca Raton, FL: CRC Press; 1997.
34. Ding C, Peng H. Minimum redundancy feature selection from microarray gene expression data. J Bioinform Comput Biol 2005;3:185–205.
35. Cristianini N, Shawe-Taylor J. An introduction to support vector machines and other kernel-based learning methods. Cambridge: Cambridge University Press; 2000.
36. Lorensen W, Cline H. Marching cubes: a high resolution 3D surface construction algorithm. ACM Siggraph Comput Graph 1987;21:163–169.
37. Koenderink JJ, van Doorn AJ. Surface shape and curvature scales. Image Vis Comput 1992;10:557–564.
38. Ter Haar Romeny BM. Biomedical image processing. In: Deserno TM, editor. New York: Springer; 2011. p 183–187.
39. Mardia KV, Kent JT, Bibby JM. Multivariate analysis. Waltham, MA: Academic Press; 1979.
40. Somorjai RL, Dolenko B, Baumgartner R. Class prediction and discovery using gene microarray and proteomics mass spectroscopy data: curses, caveats, cautions. Bioinformatics 2003;19:1484–1491.

41. Murphy K. Machine learning: a probabilistic perspective. Cambridge: MIT Press; 2012.

42. Hsu C, Chang C, Lin C. A practical guide to support vector classification. Taiwan: National Taiwan University; 2003.

43. Efron B. Estimating the error rate of a prediction rule: improvement on cross-validation. J Am Stat Assoc 1983;78:316–331.

44. Chen Y, Lin C. Combining SVMs with various feature selection strategies. In: Guyon I, Nikravesh M, Gunn S, Zadeh LA, editors. Feature extraction: foundations and applications. Berlin: Springer; 2006. p 315–324.

45. Yang G, Raschke F, Barrick TR, Howe FA. Manifold learning in MR spectroscopy using nonlinear dimensionality reduction and unsupervised clustering. Magn Reson Med 2015;74:868–878.

46. Theodoridis S, Koutroumbas K. Pattern recognition. 4th ed. San Diego: Academic Press; 2008.

47. Hanley J, McNeil B. The meaning and use of the area under a receiver operating characteristic (ROC) curve. Radiology 1982;143:29–36.

48. Gur D, Bandos A, Rockette H. Comparing areas under receiver operating characteristic curves: potential impact of the "last" experimentally measured operating point. Radiology 2008;247:12–15.

49. Wang S, Kim S, Poptani H. Diagnostic utility of diffusion tensor imaging in differentiating glioblastomas from brain metastases. AJNR Am J Neuroradiol 2014;35:928–934.

50. Jones TL. A novel magnetic resonance diffusion tensor imaging segmentation and visualisation technique for brain tumour diagnosis and surveillance. PhD Thesis, St George's, University of London; 2012.